Chemical Papers (2023) 77:7263–7275
https://doi.org/10.1007/s11696-023-02762-y

ORIGINAL PAPER

Thermally induced solid-state reaction of $Fe_2(SO_4)_3$ with NaCl or KCl: a route to β-Fe_2O_3 synthesis

Josef Kopp[1] · Karolína Kalusová[1] · Vít Procházka[1] · Petr Novák[1]

Received: 14 November 2022 / Accepted: 27 February 2023 / Published online: 17 April 2023

Abstract

β-Fe_2O_3 is a rare crystalline polymorph of the ferric oxide family with an interesting application potential, e.g., in photocatalysis. In this study, the effect of different alkali salts addition, namely NaCl and KCl, on the preparation of β-Fe_2O_3 via thermally induced solid-state reaction was investigated. Two series of samples were prepared by calcining two different mixtures, $Fe_2(SO_4)_3$ + NaCl (molar ratio 1:3) and $Fe_2(SO_4)_3$ + KCl (molar ratio 1:3) at temperatures from 350 to 700 °C. Although the addition of either alkali salt led the preparation of β-Fe_2O_3 particles in wide temperature range up to 650 °C, differences in the overall phase composition and β-Fe_2O_3 purity were observed between the two series. The addition of KCl to $Fe_2(SO_4)_3$ allowed the preparation of pure β-Fe_2O_3 (≥ 95%) in relatively wide temperature range of 450−600 °C, while in the case of NaCl, pure β-Fe_2O_3 (≥ 95%) was found only in samples calcined at 500 °C and 550 °C. Other phases could be identified as additional ferric oxide polymorphs, γ-Fe_2O_3 and α-Fe_2O_3. The in situ XRD results suggest that, in the case of NaCl + $Fe_2(SO_4)_3$ reaction, simultaneous formation of β-Fe_2O_3 and α-Fe_2O_3 may be possible between 350 and 500 °C, depending on the reaction conditions.

Keywords Iron oxides · β-Fe_2O_3 · Solid-state synthesis · Mössbauer spectroscopy · X-ray powder diffraction · In situ measurements

Introduction

The ferric oxides are a group of interesting and extensively studied materials. The ferric oxides exhibit a structural polymorphism which is responsible for their various remarkable properties. Not including the amorphous ferric oxide, four different ferric oxide crystalline polymorphs, α, β, γ and ε, were reported up to date (Cornell and Schwertmann 2003; Machala et al. 2011). The most common of the polymorphs is α-Fe_2O_3 (hematite). It founds its use in numerous applications, e.g., pigment production, (Mohapatra and Anand 2011) catalysis (Gregor et al. 2010; Ashraf et al. 2020), gas sensing (Li et al. 2018) or electrochemistry (Sivula et al. 2011). The spinel-structured γ-Fe_2O_3 (maghemite) is utilized for its superb ferrimagnetic properties, e.g., in biomedicine (Estelrich and Busquets 2018; Dadfar et al. 2019) or data storage applications (Mohapatra and Anand 2011; Ajinkya et al. 2020). The orthorhombic ε-Fe_2O_3 is investigated for its magnetic properties, specifically for its large coercive field (up to $H_c \approx 2$ T at room temperature) (Tuček et al. 2010). The ε-Fe_2O_3 magnetic thin films are of great interest for its usage as a potential high-density storage media (Tokoro et al. 2020). Lastly, β-Fe_2O_3 crystallizes in cubic structure ($a = 9.39$ Å, *Ia*3 space group) and it is the only ferric oxide polymorph that exhibits a paramagnetic behavior at room temperature (Danno et al. 2013). Recently, it has been studied as a promising candidate in applications including optoelectronics (Lee et al. 2008a, b), anodes for lithium batteries (Carraro et al. 2012) and lately photocatalysis, i.e., H_2 evolution (Zhang et al. 2017; Li et al. 2021) and pollutant degradation (Zhang et al. 2019; Fragoso et al. 2022). Additionally, the β-Fe_2O_3 was also found to be a suitable precursor for the preparation of the interesting χ-Fe_5C_2 phase (Hagg carbide), which is an active catalyst in Fischer–Tropsch synthesis (Malina et al. 2017). While both α-Fe_2O_3 and γ-Fe_2O_3 occur

This work was presented at the European Symposium on Analytical Spectrometry ESAS 2022 and17th Czech-Slovak Spectroscopic Conference held in Brno, Czech Republic on September 4–9,2022.

✉ Vít Procházka
v.prochazka@upol.cz

[1] Department of Experimental Physics, Faculty of Science, Palacký University Olomouc, 17. Listopadu 1192/12, 779 00 Olomouc, Czech Republic

naturally, the other two polymorphs, β-Fe_2O_3 and ε-Fe_2O_3 are generally synthesized in laboratory and are considered rare. So far, only a few methods have been reported for a successful preparation of these rare polymorphs in pure forms. For example, a pure ε-Fe_2O_3 phase was achieved for the first time in 2004 using a combined reverse micelle and sol–gel method (Jin et al. 2004). Preparation of pure polymorphs is usually hindered by (i) polymorphous transitions induced by high temperature or pressure that can occur during the synthesis or (ii) simultaneous formation of two different polymorphs (Machala et al. 2011).

It is known that β-Fe_2O_3, γ-Fe_2O_3 and ε-Fe_2O_3 undergo a polymorphous transition to α-Fe_2O_3 at elevated temperatures. Owing to its thermal stability, α-Fe_2O_3 is traditionally the end product of most thermal processes that involve iron oxides (Zboril et al. 2002). The exact temperature of these polymorphous transitions generally depends on various factors such as the particle size, doping, reaction atmosphere, type of precursor, etc. (Machala et al. 2011). Polymorphous transitions including all four polymorphs $\gamma \rightarrow \varepsilon \rightarrow \beta \rightarrow \alpha$ were observed in the case where the particle growth was restricted by physical barriers, e.g., by a confinement of a silica matrix (Sakurai et al. 2009). Recently, Zhang et. al. observed $\gamma \rightarrow \beta$ transition at 600 °C in the case of their electrophoretically deposited thin layers of γ-Fe_2O_3 (Zhang et al. 2022). The opposite $\beta \rightarrow \gamma$ transition was observed by Lee et al. in the case of their hollow β-Fe_2O_3 nanoparticles (Lee et al. 2008a, b). Although β-Fe_2O_3 was found to be more thermodynamically stable than ε-Fe_2O_3, the direct transition $\varepsilon \rightarrow \beta$ remains a question of debate. According to Machala et al. (2011), the coexistence of both phases that was reported in the past (Sakurai et al. 2009) might have been the product of simultaneous formation. The simultaneous formation of α-Fe_2O_3 and γ-Fe_2O_3 was reported, for example, in the case of the thermal decomposition of $FeC_2O_4{\cdot}2H2O$, while the simultaneous formation of α-Fe_2O_3 and β-Fe_2O_3 was observed during the thermal decomposition $Fe_4(Fe(CN)_6)_3$ (Hermanek and Zboril 2008; Machala et al. 2013). The ratio of the polymorphs was found to be dependent on the precursor thickness during calcination and particle size, respectively. For more detailed information about polymorphous transitions of ferric oxide the readers are referred to a review by Machala et al. (2011).

Concerning β-Fe_2O_3, several synthesis methods were reported for the preparation of either pure or high-fraction β-Fe_2O_3, including chemical vapor hydrolysis (Bonnevie Svendsen 1958; Kumar and Singhal 2007; 2009), condensation (CVC) (Lee et al. 2004; Lee et al 2008a, b), spray pyrolysis (Li et al. 2021), hydrothermal route, (Rahman et al. 2011) microwave-assisted solvothermal route (Ramya and Mahadevan 2012) and solid-state reaction involving the thermal decomposition of a suitable iron salt, e.g. β-Fe_2O_3 was reported among the products of thermally induced decomposition of iron(III) hexacyanoferrate(II) microcrystals (20–50 μm) or iron(III) sulfate (Machala et al. 2013; Zboril et al. 1999a, b, 2003). However, most of these reaction routes provided β-Fe_2O_3 in mixture with other ferric oxide polymorphs, e.g. α-Fe_2O_3.

Another method for the preparation of pure β-Fe_2O_3 is the solid-state reaction that was first reported by Ikeda et al. (1986) and comprises a calcination of $Fe_2(SO_4)_3$ and NaCl mixture with subsequent isolation of ferric particles by decantation. According to Ikeda et al. (1986), the $Fe_2(SO_4)_3 + NaCl$ reaction starts with the formation of $NaFe(SO_4)_2$ double sulfate. The β-Fe_2O_3 particles are formed at 500 °C following the equation:

$$3NaFe\left(SO_4\right)_2 \rightarrow Na_3Fe\left(SO_4\right)_2 + \beta\text{-}Fe_2O_3 + 3SO_3,$$

Later, Zboril et al. (1999a, b), who also studied the $Fe_2(SO_4)_3 + NaCl$ solid-state reaction, suggested that β-Fe_2O_3 formation follows 2 different reaction pathways; (i) between 400−440 °C β-Fe_2O_3 is formed directly through the decomposition of $Fe_2(SO_4)_3$:

$$30NaCl + 10Fe_2\left(SO_4\right)_3 + 15/2O_2 \rightarrow 6Na_3Fe\left(SO_4\right)_3 + 4NaFe\left(SO_4\right)_2 + 5\beta\text{-}Fe_2O_3 + 4Na_2SO_4 + 15Cl_2.$$

and (ii) above 440 °C β-Fe_2O_3 is also formed by the decomposition of the two double sulfates $NaFe(SO_4)_2$ and $Na_3Fe(SO_4)_3$. According to Zboril et al. (1999a, b), a secondary reaction, i.e., β-$Fe_2O_3 \rightarrow$ α-Fe_2O_3 polymorphous transition, accompanied the primary reaction from its onset at 400 °C and was responsible for the presence of α-Fe_2O_3 fraction in their samples. More recently, Danno et al. (2010; 2013) reported the preparation of pure β-Fe_2O_3 particles via solid-state reaction. Contrary to both Ikeda et al. (1986) and Zboril et al. (1999a, b), they calcined a mixture of NaCl and $NaFe(SO_4)_2$. Pure β-Fe_2O_3 was prepared regardless of the reactants ratio already at 350 °C, which further indicated the $NaFe(SO_4)_2$ important role in the process.

Although the calcination of $Fe_2(SO_4)_3 + NaCl$ for the preparation of β-Fe_2O_3 is known, to the best of our knowledge, the exact role of the alkali salt has not been fully explained. In this article we further investigate the role of the alkali ion addition on the preparation of β-Fe_2O_3 by comparing the solid-state reaction of two different mixtures: $Fe_2(SO_4)_3 + NaCl$ and $Fe_2(SO_4)_3 + KCl$ in the 1:3 ratio at different temperatures. The phase composition and purity of the prepared β-Fe_2O_3 powder were verified by transmission Mössbauer spectroscopy (TMS) and powder X-ray diffraction (XRD). The reactions processes were also studied by an in situ XRD. We believe the presented study brings further insight into the formation of the rare

β-Fe_2O_3 polymorph as well as the solid-state reactions in general.

Experimental

Chemicals

Ferric sulfate hydrate ($Fe_2(SO_4)_3 \cdot nH_2O$), sodium chloride (NaCl) and potassium chloride (KCl) were all purchased from PENTA ltd. Prior to its use, $Fe_2(SO_4)_3 \cdot nH_2O$ was dehydrated for 2 h at 400 °C in N_2 atmosphere in accordance with work of Zboril et al. (1999a, b). KCl and NaCl large microcrystals were milled at 30 Hz for 30 min in MILLMIX 20 vibratory ball mill (DOMEL) to obtain a superfine powder (1−1.5 µm) and to exclude the effect of particle size when comparing the two salts. For milling, 1 g of the respective salt was put into 10 ml hard steel grinding jar together with a single 10 mm hard steel ball (Fig. S 1). Otherwise, the chemicals were used without any further purification.

Synthesis

Two separate mixtures comprising NaCl or KCl and dehydrated $Fe_2(SO_3)_4$ in the molar ratio 3:1 were prepared and further homogenized in MILLMIX 20 ball mill (DOMEL) for additional 20 min at 30 Hz. Several milling runs were conducted to prepare sufficient amount of both mixtures. For each milling run, 0.5 g of dehydrated $Fe_2(SO_3)_4$ and the appropriate amount of salt were enclosed in 10 ml hard steel grinding jar with a single 10 mm ball. Both prepared mixtures were subsequently calcined in pre-heated LAC LE/05 laboratory furnace with HP40 controller at selected temperatures for 1 h in static air atmosphere. Samples (approximately 300 mg) were calcined in ceramic combustion boats (Fig. S 2). The temperature range was set in accordance with previous works, i.e., 350−700 °C (Ikeda et al. 1986; Zboril et al. 1999a, b; Danno et al. 2010). In overall, 16 samples with 50 °C temperature step divided into two series were prepared. The used alkali ion and calcination temperature were used for naming the individual samples, i.e., Na350, …, Na700 and K350, …, K700. The samples were put into furnace in pairs (one sample from each mixture) to guarantee the same reaction conditions. Products of calcination were mixed with deionized water and left to sediment. Any remaining sulfates were dissolved and removed by decantation. The isolated iron oxide particles were left to dry in ambient atmosphere. The washing step could not be included in the case of in situ measurements.

Experimental techniques

X-ray powder diffraction (XRD)

Structural analysis of the prepared oxides was performed with X-ray powder diffraction (XRD). Diffraction patterns in 2θ range from 10° to 100° with step of 0.02° were measured at ambient conditions using D8 ADVANCE diffractometer (Bruker) with Bragg–Brentano geometry, LYNXEYE position sensitive detector and Co tube. The 0.6 mm divergence slit and 2.5° axial Soller slits were implemented to primary beam path. The Fe Kβ filter and 2.5° axial Soller slits were present at the secondary beam path. In situ investigations of the solid-state reactions were performed in XRD in situ chamber XRK900 (Anton Paar) under constant flow of synthetic air. The investigation has been carried out within temperature range of 30−750 °C. The temperature step was set to 10 °C. Each measurement step lasted approximately 15 min. Instrument settings were identical to those used for ambient conditions except for Soller slits, which were removed. Rietveld refinement of the diffraction patterns was conducted in MAUD program (Lutterotti 2010). The lines positions shown in Figures below were calculated in VESTA software using the Open Crystallography database (COD) CIF files (Momma and Izumi 2011; Grazulis et al. 2009).

Transmission ^{57}Fe Mössbauer spectroscopy (TMS)

Transmission ^{57}Fe Mössbauer spectroscopy (TMS) analyses at both room and low temperature were performed using OLTWINS dual spectrometer developed at Palacký University Olomouc, Czech Republic (Novák et al. 2022; Procházka et al. 2020). The low temperatures were achieved with cryostat (Montana Instruments). The ^{57}Co embedded in rhodium matrix was employed as a radioactive source. The recorded transmission spectra were evaluated with MossWinn 4.0 software (Klencsár et al. 1996). The isomer shift values were calibrated with respect to that of α-iron at room temperature.

Scanning electron microscopy (SEM)

The SEM images of the prepared oxides were recorded with VEGA3 LMU scanning electron microscope equipped with secondary electron Everhart–Thornley detector (Tescan). The accelerating voltage was set to 30 kV for all images. To increase the conductivity, the samples were covered with a thin layer of cobalt (20 nm) using Q150T ES sputtering device (Quorum Technologies).

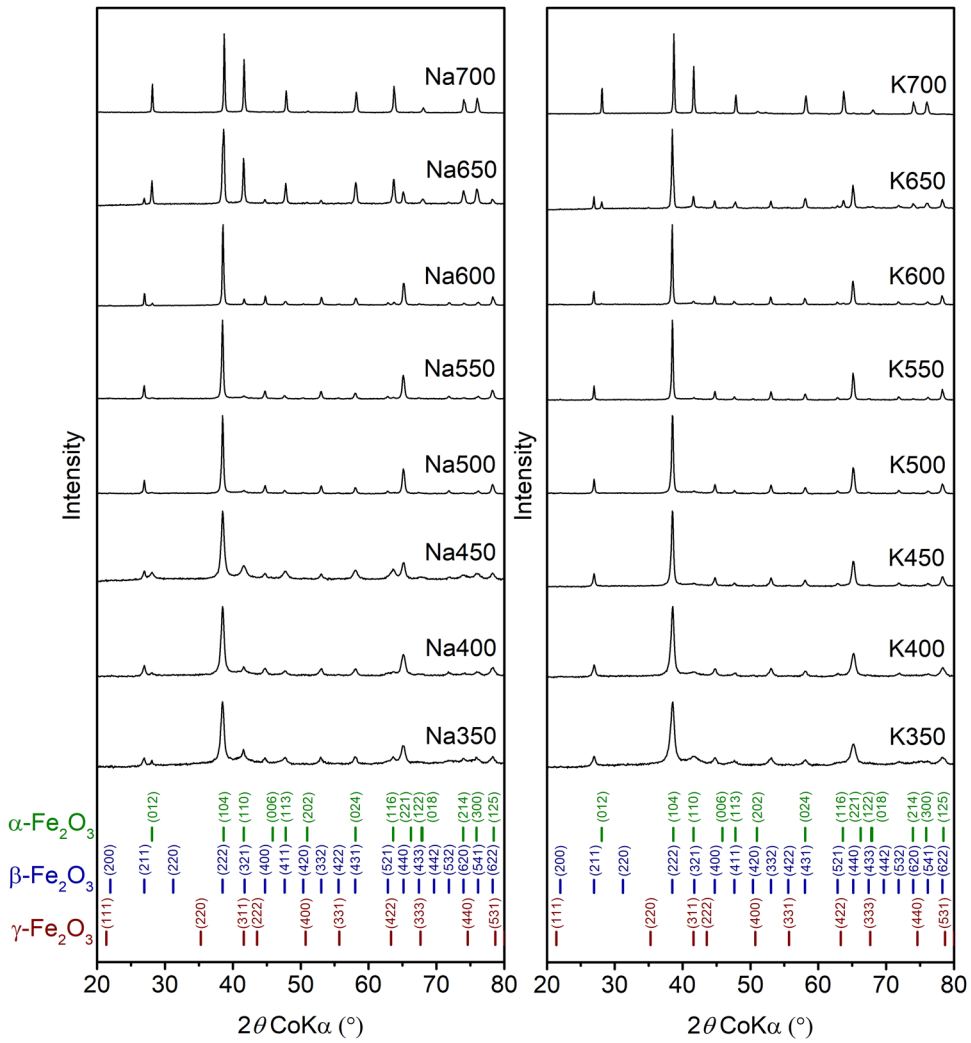

Fig. 1 Diffraction patterns in 2θ range 20−80° of washed-out samples for NaCl series (left) and KCl series (right). Vertical lines show the positions of diffraction maxima of α-Fe_2O_3 (green, COD1546383), β-Fe_2O_3 (blue, COD1514107) and γ-Fe_2O_3 (brown, COD9006316). Data were normalized with respect to the maximum amplitude

Results and discussion

The XRD patterns of the samples of both series are displayed in Fig. 1. The patterns show the successful preparation of β-Fe_2O_3 (blue), whose diffraction lines were found in all samples, except for Na700 and K700. At 700 °C, both samples contained exclusively α-Fe_2O_3 lines (green). The α-Fe_2O_3 amount in other samples varied with temperature. The α-Fe_2O_3 diffraction lines of different intensity could be visible in almost all NaCl series samples (except Na500, Na550). On the other hand, no clearly visible diffraction lines of α-Fe_2O_3 were found in KCl series samples up to 600 °C.

Figure 2 displays the 25−30° range zoom in of the diffraction patterns and compares the intensities of α-Fe_2O_3 reflection (012) (green) and β-Fe_2O_3 reflection (211) (blue) between the two series. All data were normalized with respect to the amplitude of (211) reflection peak. It is evident that KCl series contained less α-Fe_2O_3 in overall. The data also clearly show the evolution of the linewidth signalizing the increasing degree of crystallinity with the rising temperature.

Apart from α-Fe_2O_3, the nature of the background observed in samples Na350, Na450, K350 and K400 suggested the presence of another poorly crystalline phase. Fig. 3 shows the Rietveld fit for samples (a) Na350 and (b) K350. The broad peak at $2\theta \approx 41.8°$ could be the (311) reflection coming from very small crystallites of γ-Fe_2O_3 (see Fig. 3). Superparamagnetic nanoparticles of γ-Fe_2O_3 were previously observed during the early stages of $Fe_2(SO_4)_3$ thermal decomposition by Zboril et al. (2003). No additional diffraction lines, other than those of α-Fe_2O_3, β-Fe_2O_3 and γ-Fe_2O_3 were observed, signalizing that the other calcination products were successfully washed out.

It should be noted that the two most intensive reflection of α-Fe_2O_3, i.e. (104) and (110) nearly overlap with the β-Fe_2O_3 reflections (222) and (321), making the distinguishing of very low α-Fe_2O_3 amounts in the patterns challenging, especially in the case of broad peaks. Additionally, the reflection positions of α- (110) and β- (321) also nearly coincide with

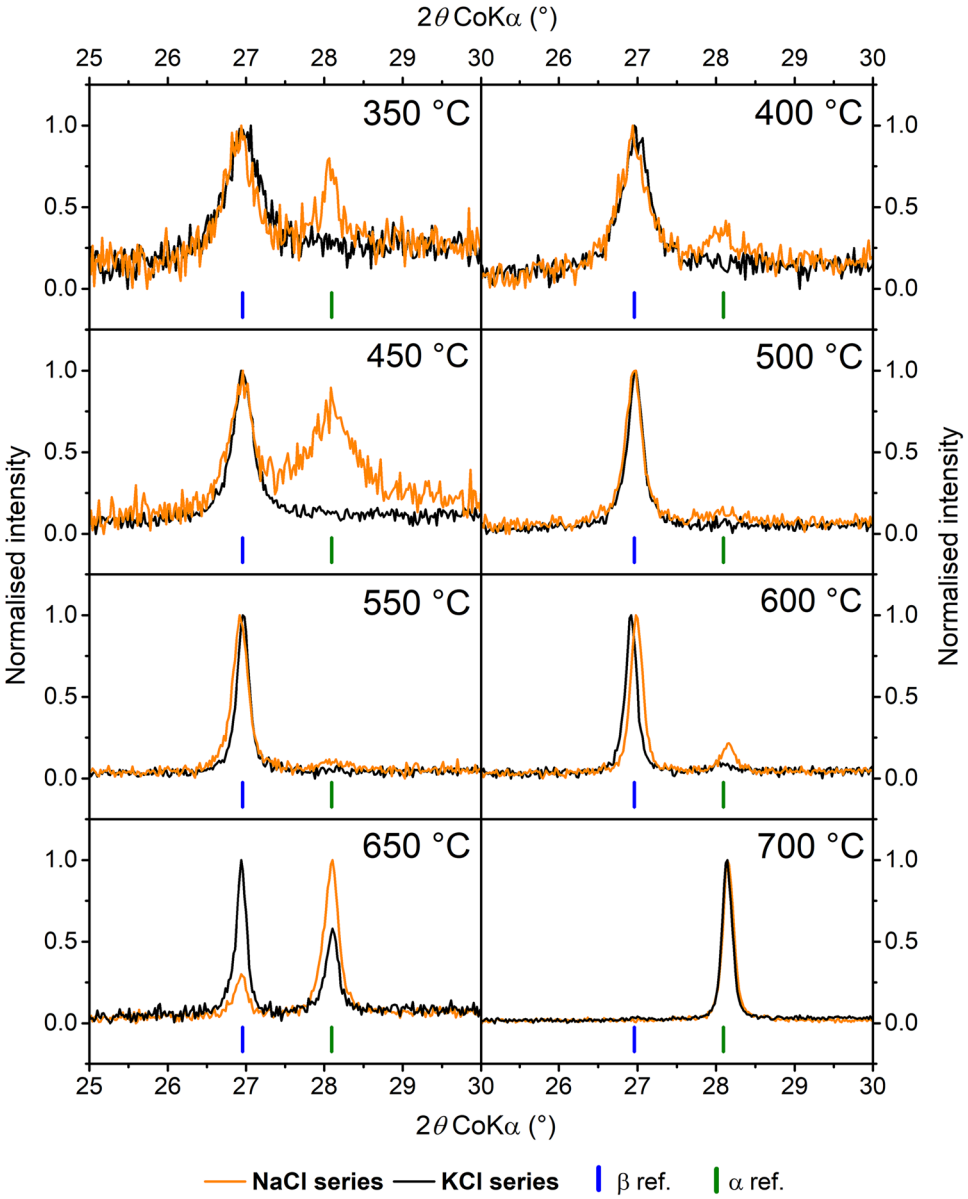

Fig. 2 Comparison of the XRD patterns in the 25−30° range between the NaCl (orange) and KCl (black) series of samples. Vertical lines mark the position of the (211) reflection (β-Fe_2O_3, blue, COD154107) and (012) reflection (α-Fe_2O_3, green, COD1546383)

the γ-Fe_2O_3 reflection (311), i.e., its most intensive diffraction line. All Rietveld fits are in Supplementary data (Fig. S3−S18). The phase compositions determined by Rietveld analysis for both series are shown in Fig. 4 (solid lines, full symbols) and Table S 1. The phase composition obtained from the relative area (RA) of the components in Mössbauer spectra (dash lines, hollow symbols) is shown as well.

Figure 5 shows the representative room temperature spectra (RTMS) of samples Na500 (a) and K500 (b). Other spectra and their respective fits could be found in Supplementary Data (Fig. S 19−S 32). The complete list of hyperfine parameters and RA values of all samples could also be found in Supplementary Data as a part of Table S 2. Most of the spectra exhibited two doublets that could be ascribed to non-equivalent crystallographic sites (d) and (b) of β-Fe_2O_3. The observed doublets reflect the paramagnetic behavior of β-Fe_2O_3. Similarly to XRD, a sextet of α-Fe_2O_3 could be found in both series at higher temperatures (600− 700 °C) and also in spectra of samples Na350, Na400, Na450. The amount of α-Fe_2O_3 was particularly high in Na450. The large hyperfine magnetic field of $B_{hf} \approx 51$ T is typical for α-Fe_2O_3. Different magnetic behavior allows facile differentiation of α-Fe_2O_3 and β-Fe_2O_3 in the Mössbauer spectra.

Contrary to XRD patterns, a small doublet component could be also identified in samples K700 and Na700 (Fig. S 25 and Fig. S 32), presumably belonging to the remaining β-Fe_2O_3, even though no β-Fe_2O_3 diffraction lines could be found in the respective XRD patterns. In most of the samples, the observed RA values of the two β-Fe_2O_3 doublet components match the theoretical (d): (b) ratio of 3: 1 (Table

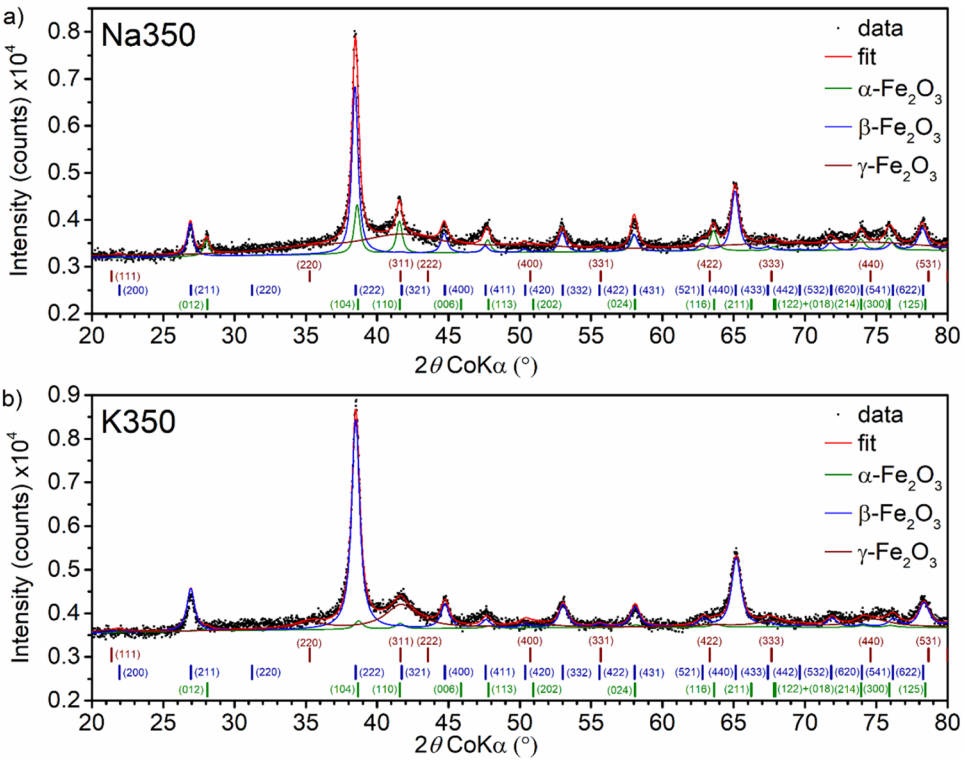

Fig. 3 Diffraction pattern and Rietveld fit for samples **a** Na350 and **b** K350. Vertical bars mark the positions of the individual reflections for α-Fe_2O_3 (green, COD1546383), β-Fe_2O_3 (blue, COD1514107) and γ-Fe_2O_3 (brown, COD9006316)

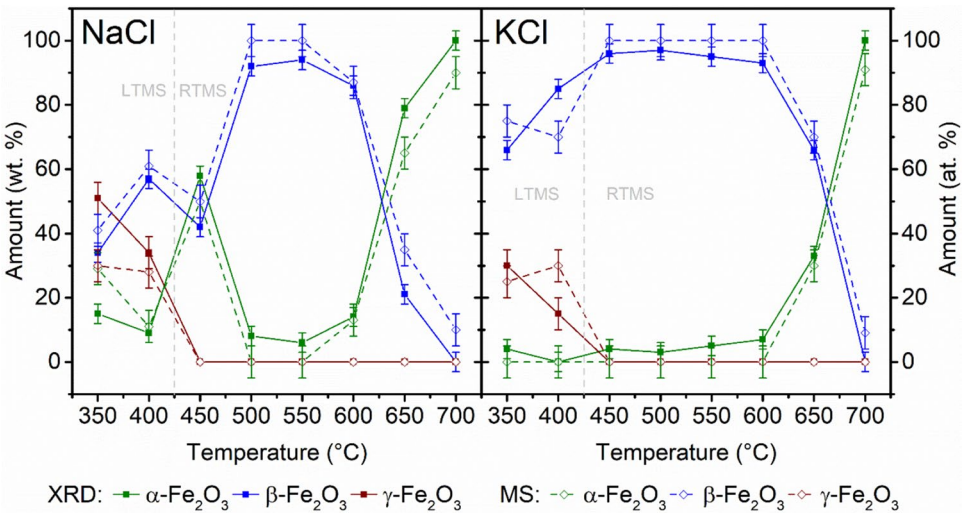

Fig. 4 Phase composition obtained from Rietveld refinement (solid) and from RA of Mössbauer spectra (dash) for both NaCl series (left) and KCl series (right). The amount of β-Fe_2O_3 in MS results is a sum of (d) and (b) sites RA. Results of low temperature MS (LTMS) are displayed for samples Na350, Na400, K350, K400

S 1). A different ratio was observed for samples Na350, K350 and K400, i.e., samples where the XRD patterns indicated the presence of poorly crystalline phase. However, such phase (e.g., superparamagnetic γ-Fe_2O_3 or amorphous ferric oxide) would exhibit similar hyperfine parameters to β-Fe_2O_3 at room temperature (Machala et al. 2007).

Therefore, the spectra of samples Na350, Na400, K350 and K400 were recorded at 22 K and they are shown in Fig. 6a–d. Up to four sextet components could be identified in the low temperature spectra (LTMS), implying that β-Fe_2O_3 underwent a magnetic transition below Néel temperature (Malina et al. 2015). Thus two of the sextets could be ascribed to (d) and (b) sites of β-Fe_2O_3, respectively. A wide sextet with $B_{hf} > 53$ T observed only in samples Na350 and Na400 belongs probably to hematite, which was also identified in XRD patterns. The last sextet component with hyperfine parameters $\delta = 0.50-0.54$ mm/s and $B_{hf} = 44.8-45.7$ T then confirmed the presence of another iron containing phase. This phase might be superparamagnetic γ-Fe_2O_3 below its blocking temperature. The hyperfine parameters of LTMS are in Table 1. In the fitting model, the isomer shift and quadrupole splitting of

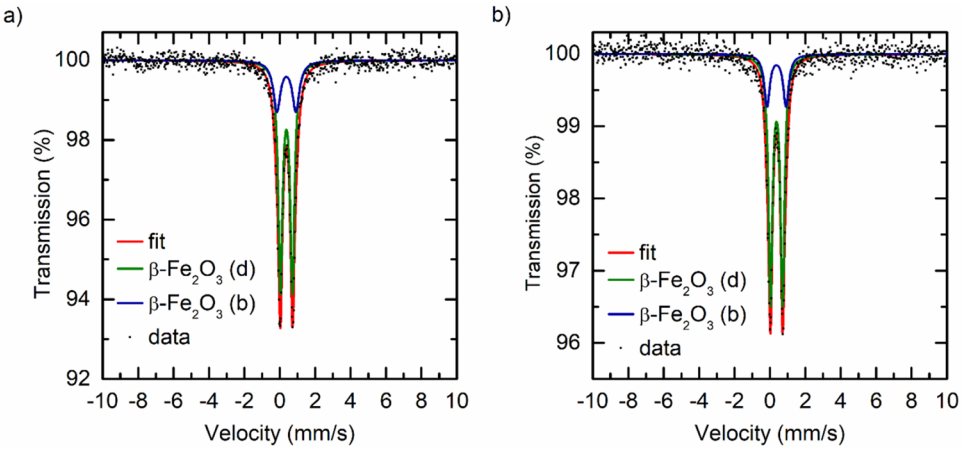

Fig. 5 Representative RT Mössbauer spectra of samples Na500 **a** and K500 **b**

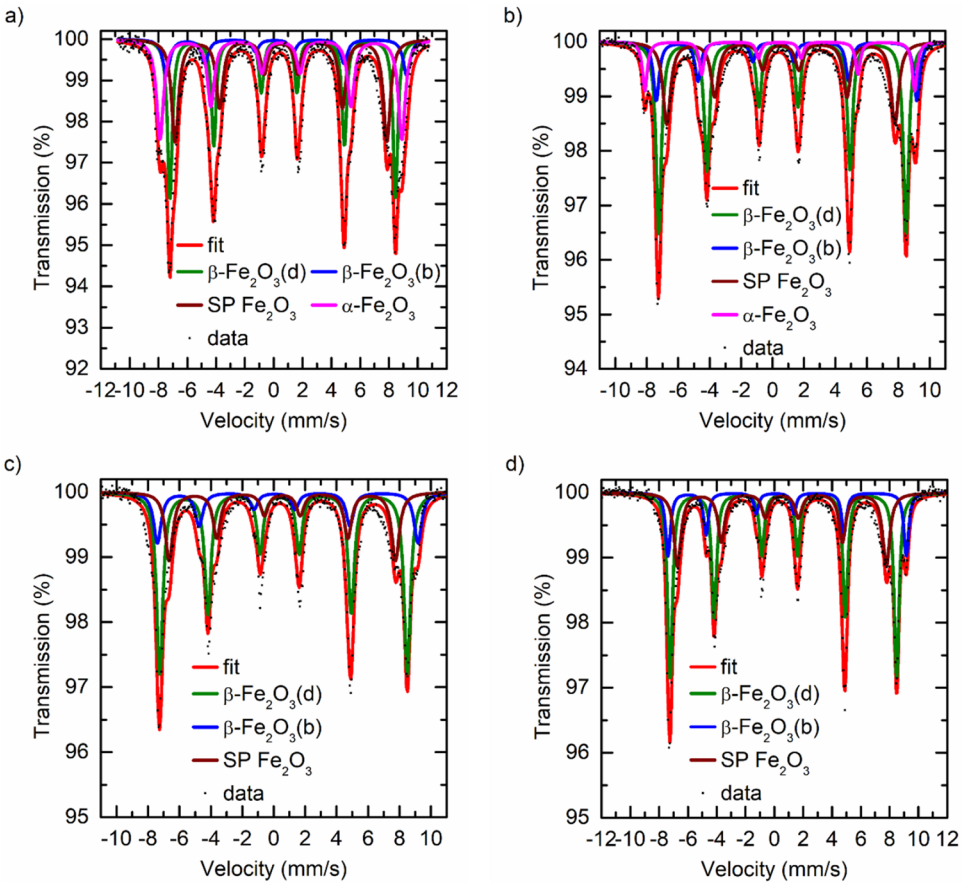

Fig. 6 Low temperature Mössbauer spectra (22 K) of samples **a** Na350, **b** Na400, **c** K350 and **d** K400

β-Fe_2O_3 (d) and (b) sites were fixed to values found in Malina et al. (2015).

The results displayed in Fig. 4 show that the Rietveld analysis phase composition correlates relatively well with the one obtained from Mössbauer spectroscopy. The differences can be observed at temperatures 350 °C and 400 °C. These may be connected with either a challenging quantification of poorly crystalline phase in XRD or with a chosen fitting model of low temperature Mössbauer spectra. Comparing the two series, the results show that pure β-Fe_2O_3 (≥ 95%) was found in different temperature ranges. In NaCl series the pure β-Fe_2O_3 was found only in samples Na500 and Na550, while in the case of KCl series the pure β-Fe_2O_3 was found in a wider temperature range. The observed results from both TMS and XRD also indicate that α-Fe_2O_3 in the samples is a product of two different processes. At high temperatures (> 600 °C) the majority of α-Fe_2O_3 is the product of β-Fe_2O_3 → α-Fe_2O_3 transformation. This transformation was observed for both NaCl and KCl series of samples. On the other hand, the clear presence of α-Fe_2O_3 in

Table 1 Hyperfine parameters and RA values for spectra of Na350, Na400, K350 and K400 recorded at 22 K

Sample	Phase	$\delta \pm 0.02$ (mm/s)	$\Delta E_Q \pm 0.02$ (mm/s)	$B_{hf} \pm 0.3$(T)	RA ± 5 (%)
Na350-22 K	β-Fe_2O_3 (d)	0.50*	0.25*	48.6	31
	β-Fe_2O_3 (b)	0.47*	0.84*	51.8	10†
	SP Fe_2O_3	0.50	–	45.7	29
	α-Fe_2O_3	0.50	–	52.1	29
Na400-22 K	β-Fe_2O_3 (d)	0.50*	0.25*	48.9	46
	β-Fe_2O_3 (b)	0.47*	0.84	51.5	15†
	SP Fe_2O_3	0.52	–	45.1	28
	α-Fe_2O_3	0.45	–	53.4	11
K350-22 K	β-Fe_2O_3 (d)	0.50*	0.25*	48.9	56
	β-Fe_2O_3 (b)	0.47*	0.84*	51.5	19†
	SP Fe_2O_3	0.54	–	44.8	25
K400-22 K	β-Fe_2O_3 (d)	0.50*	0.25*	48.9	52
	β-Fe_2O_3 (b)	0.47*	0.84*	51.3	18†
	SP Fe_2O_3	0.52	–	45.1	30

δ – isomer shift, ΔE_Q – quadrupole splitting, B_{hf} – hyperfine magnetic field, RA – relative area

* – fixed (Malina et al. 2015), † – bound to (d) site with factor 0.333

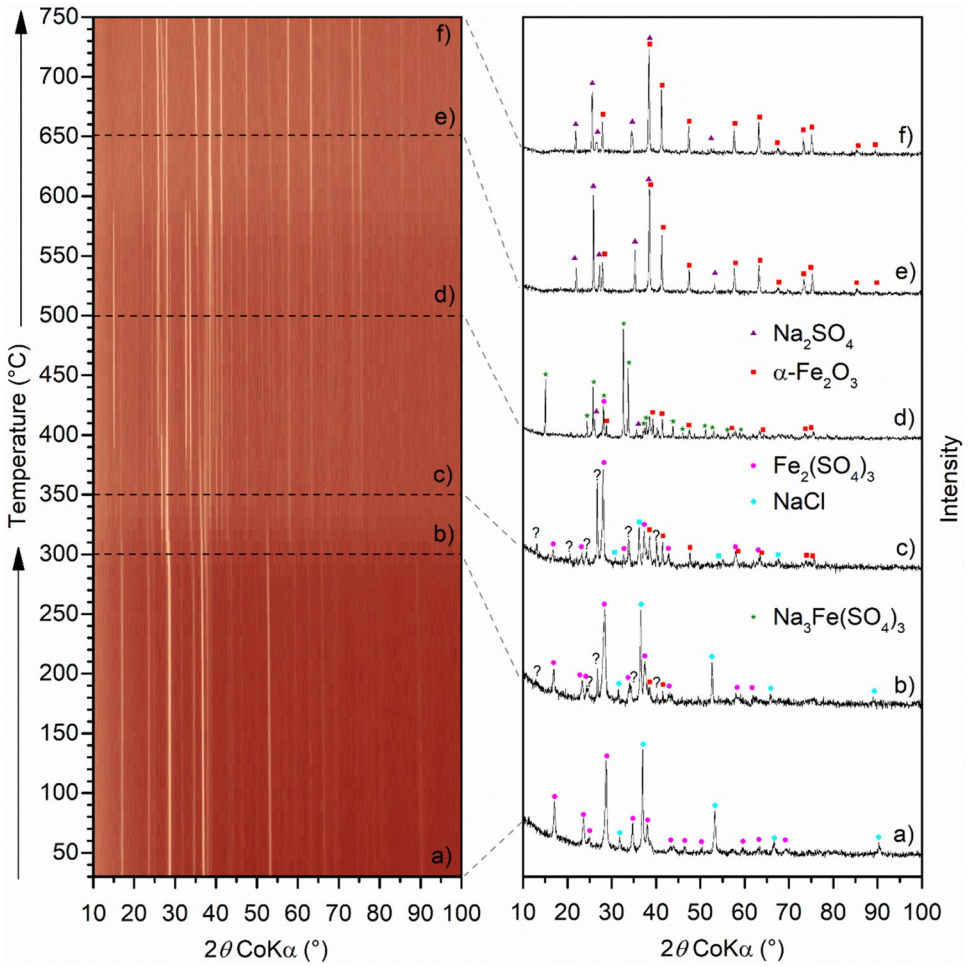

Fig. 7 In situ XRD map of $NaCl + Fe_2(SO_4)_3$ calcination and selected patterns at **a** 30 °C, **b** 300 °C, **c**) 350 °C, **d** 500 °C, **e** 650 °C and **f** 750 °C

samples Na350, Na400 and Na450 is most probably a result of a different reaction process. To investigate the course of these thermally induced solid-state reactions further, both mixtures were studied with in situ XRD. Figure 7 shows the resultant map and selected XRD patterns for the calcination of $NaCl + Fe_2(SO_4)_3$ mixture.

All diffraction peaks observed up to 290 °C could be ascribed to the used precursors, i.e., $Fe_2(SO_4)_3$ and NaCl. A gradual disappearance of NaCl lines accompanied by a significant shift to the left of the $Fe_2(SO_4)_3$ lines was observed between 300 °C and 350 °C. Diffraction patterns also displayed additional lines belonging to α-Fe_2O_3 and to an unidentified phase, whose lines gradually grew in intensity. Unfortunately, the overall complexity of the patterns, thermal effects, and low statistics did not allow the reliable phase identification in all patterns. Further increase in the temperature (> 350 °C) revealed slightly rising intensity of α-Fe_2O_3 lines accompanied by the appearance of $Na_3Fe(SO_4)_3$ lines which became dominant rapidly. Around 500 °C the lines corresponding to an unidentified phase disappeared from the patterns. At 570 °C, i.e., thermal stability threshold of both compounds, the intensity of $Fe_2(SO_4)_3$ and $Na_3Fe(SO_4)_3$ lines started to decrease, while the intensity of α-Fe_2O_3 and Na_2SO_4 (polymorph I) increased significantly. At 600 °C the patterns contained only the lines of α-Fe_2O_3 and Na_2SO_4 (polymorph I), which remained in the patterns until 750 °C, i.e., the highest attained temperature. Nonetheless, in none of the diffraction patterns within 30−750 °C temperature range, the peaks belonging to β-Fe_2O_3 could be identified, implying that the reaction in the in situ experiment proceeded differently from the ex situ experiments, probably because of the different rate at which the temperature increased.

On the other hand, the diffraction peaks of β-Fe_2O_3 were identified in the in situ XRD patterns of $KCl + Fe_2(SO_4)_3$ mixture (Fig. 8). The patterns corresponding to temperatures below 250 °C contained only lines of KCl and $Fe_2(SO_4)_3$. The lines of both precursor salts disappeared between the 250 °C and 260 °C, while a new set of diffraction lines appeared. Contrary to $NaCl + Fe_2(SO_4)_3$ map, this first transition was very rapid occurring within the two subsequent measurements. Unfortunately, we could not reliably ascribe these new lines to any meaningful phase, e.g., to $KFe(SO_4)_2$. The next structural transition was observed approximately at 390 °C, where the lines of the

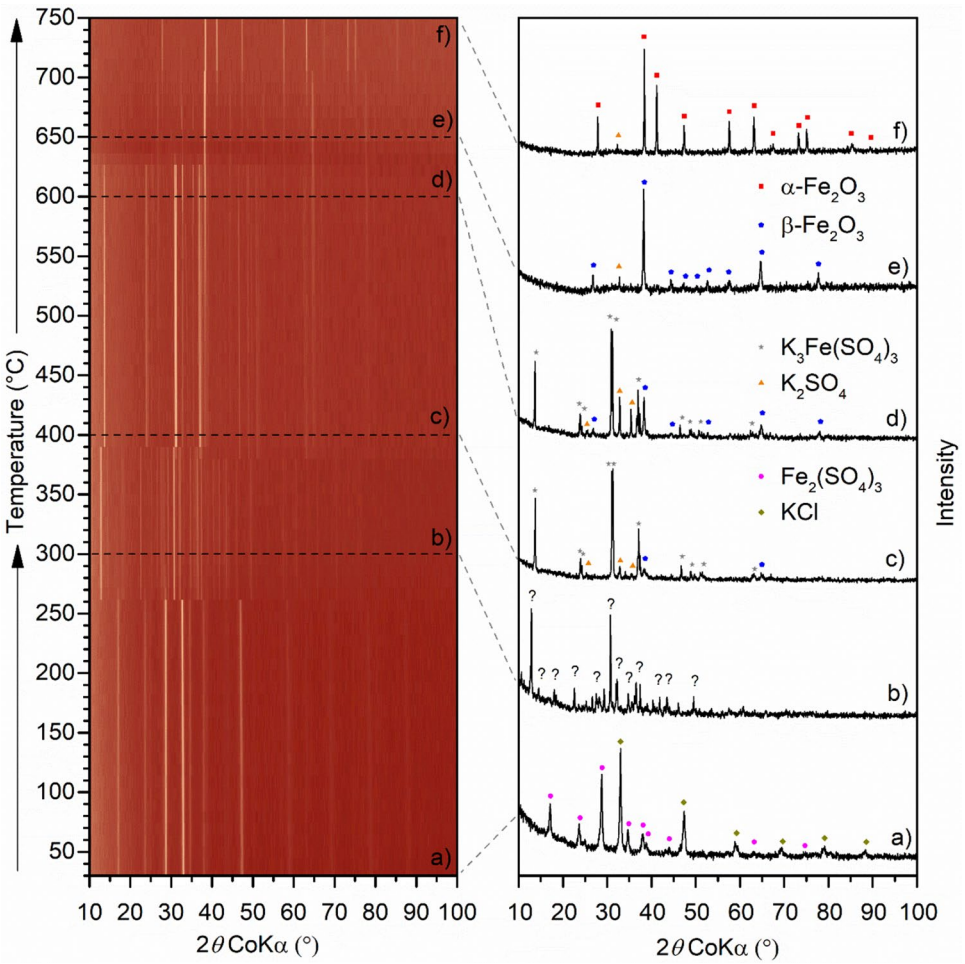

Fig. 8 In situ XRD map of $KCl + Fe_2(SO_4)_3$ calcination and selected patterns at **a** 30 °C, **b** 300 °C, **c** 400 °C, **d** 600 °C, **e** 650 °C and **f** 750 °C.

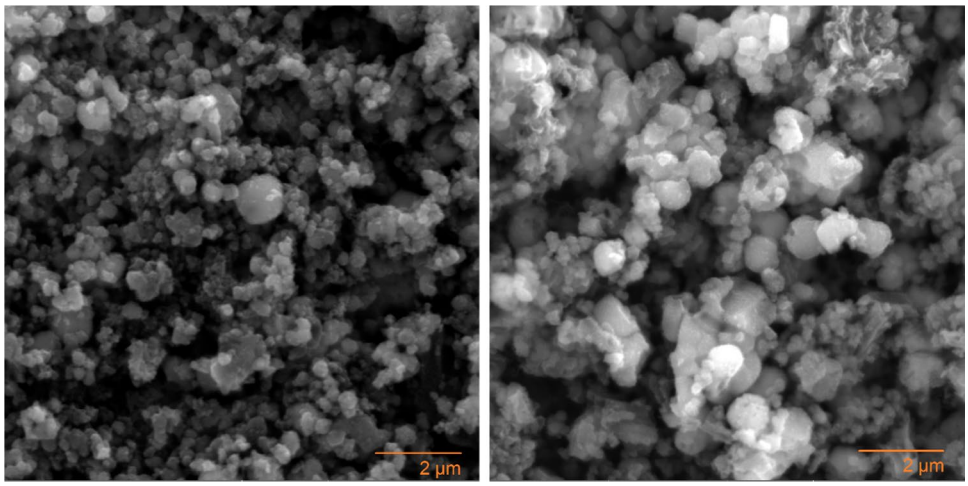

Fig. 9 SEM images of samples Na500 (left) and K500 (right)

unidentified phase rapidly vanished and the new lines of β-Fe_2O_3, K_2SO_4 and $K_3Fe(SO_4)_3$ could be identified. The intensity of β-Fe_2O_3 peaks increased with the increasing temperature. Between 630−680 °C (after reaching the melting point of $K_3Fe(SO_4)_3$) diffraction peaks of β-Fe_2O_3 dominated the XRD patterns. At 680 °C the start of the final β-$Fe_2O_3 \rightarrow$ α-Fe_2O_3 transition was observed. The onset of this final reaction correlates well with the previously published results, e.g. Malina et al. (2014).

In overall, it could be seen that the addition of the alkali salt significantly lowers the starting temperature for the formation of ferric oxides. The pure $Fe_2(SO_4)_3$ decomposes between 500 °C and 570 °C (Tagawa 1984; Siriwardane et al. 1999) while in the case of mixtures containing alkali salts the ferric oxides could be observed already between 350−390 °C. The differences in the results between the in situ experiments and the two series suggest that the observed solid-state reactions are very complex, and that, apart from temperature, other reaction conditions, e.g., heating rate, might play an important role in the formation of ferric oxides. Both different conditions and poor crystallinity might explain the absence of γ-Fe_2O_3 during the in situ experiments. However, the absence of γ-Fe_2O_3 diffraction lines in the in situ maps also hinders any attempt to draw conclusions about possible γ-$Fe_2O_3 \rightarrow$ β-Fe_2O_3 or γ-$Fe_2O_3 \rightarrow$ α-Fe_2O_3 transitions. The differences between the results of NaCl + $Fe_2(SO_4)_3$ in situ experiment and those of the NaCl series, specifically the absence of β-Fe_2O_3, could be explained that α-Fe_2O_3 a β-Fe_2O_3 are products of two different reaction pathways and the preference of either pathway in the overall NaCl + $Fe_2(SO_4)_3$ reaction is determined by the actual temperature, thus indirectly also by a heating rate. Simultaneous formation of different polymorphs in the case of the thermal decomposition of pure $Fe_2(SO_4)_3$ was observed before. On the other hand, in the case of using KCl, the crystallization of β-Fe_2O_3 was observed in both types of conducted experiments, suggesting that in the presence of K the β-Fe_2O_3 formation pathway is favored regardless of the studied reaction conditions. Unfortunately, the complexity of the in situ diffraction patterns did not allow the identification of some intermediate phases, which would help to discern the involved reactions. Contrary to other authors, we could not reliably identify $NaFe(SO_4)_2$ (or $KFe(SO_4)_2$) as the source of β-Fe_2O_3. Nonetheless, we believe that the formation of an intermediate phase through the displacement reaction between the alkali salt ion and Fe is crucial for the crystallization of β-Fe_2O_3 and the abundance of α-Fe_2O_3 is indirectly connected to an unreacted $Fe_2(SO_4)_3$ which could be observed in the NaCl + $Fe_2(SO_4)_3$ in situ experiment map up to 570 °C.

Lastly, the morphology of the prepared samples was observed with SEM. The representative images of both series are shown in Fig. 9, i.e., images of Na500 (left) and K500 (right). Images of other samples can be found in Supplementary Information (Fig. S 33–S 48). The observed particles varied in size significantly. The size of smallest objects observed in samples Na500 and K500 was around 200 nm while the size of the largest objects was up to 1 µm. An overall gradual growth of the particles with the increasing temperature could be seen as well, especially in the case of KCl series. Moreover, similarly to Ikeda et al. (Ikeda et al. 1986), the final β → α transition was also accompanied by a change in particles morphology, from irregular to rod-shaped (Fig S 40, Fig S 47 and Fig S 48).

Conclusions

The solid-state reactions of $Fe_2(SO_4)_3$ with alkali chloride salts, namely NaCl and KCl were observed to investigate the effect of the salt presence on the formation of rare β-Fe_2O_3. In order to exclude possible influence of factors such as particles size and thermal treatment variation in the comparison of two solid-state reactions, the two mixtures

($Fe_2(SO_4)_3$ + Na(K)Cl, 1:3) were crushed in the vibratory ball mill and then calcined simultaneously. In both cases the formation of ferric oxides started at a relatively lower temperature compared to the decomposition temperature of pure $Fe_2(SO_4)_3$. Characterization of the samples calcined in the pre-heated furnace showed that particles of β-Fe_2O_3 were prepared in the wide range of temperatures ≈ 350−650 °C. Nonetheless, certain samples contained additional ferric oxide polymorphs. At lower temperatures, particularly in the samples calcined at 350 °C and 400 °C, the presence of a poorly crystalline phase, possibly γ-Fe_2O_3, was confirmed with the low temperature Mössbauer spectroscopy. At higher temperatures (> 600 °C) the β-Fe_2O_3 → α-Fe_2O_3 transition was observed for both series. In the case of the NaCl series, α-Fe_2O_3 was also found in samples Na350, Na400 and Na450. By studying both solid-state reactions using in situ XRD, we believe that in the case of these samples α-Fe_2O_3 and β-Fe_2O_3 were formed simultaneously by two different processes whose reaction rates are governed by the reaction conditions. In the case of using KCl, the samples did not contain any significant amount α-Fe_2O_3 up to 650 °C suggesting that second reaction pathway leading to α-Fe_2O_3 was suppressed. Unfortunately, the complexity of the in situ diffraction patterns reactions did not allow us to reliably identify the intermediate phases that were involved the crystallization of β-Fe_2O_3. In overall, the use of KCl allowed to prepare pure β-Fe_2O_3 (> 95%) in the wide temperature range of 450−600 °C and it also precedes the contamination with α-Fe_2O_3 that is possible with the use of NaCl.

Supplementary Information The online version contains supplementary material available at https://doi.org/10.1007/s11696-023-02762-y.

Acknowledgements The authors gratefully acknowledge the financial support from the internal IGA grant of Palacký University (IGA_PrF_2022_003). Authors would like to thank Vítězslav Heger for his help with XRD data acquisition and Jiří Pechoušek for conducting low temperature measurements.

Funding Open access publishing supported by the National Technical Library in Prague.

Declarations

Conflict of interest On behalf of all authors, the corresponding author states that there is no conflict of interest.

References

Ajinkya N, Yu X, Kaithal P, Luo H, Somani P, Ramakrishna S (2020) Magnetic iron oxide nanoparticle (IONP) synthesis to applications: present and future. Materials 13(20):1–35. https://doi.org/10.3390/ma13204644

Ashraf M, Khan I, Usman M, Khan A, Shah SS, Khan AZ, Saeed K et al (2020) Hematite and magnetite nanostructures for green and sustainable energy harnessing and environmental pollution control: a review. Chem Res Toxicol 33(6):1292–1311. https://doi.org/10.1021/acs.chemrestox.9b00308

Bonnevie Svendsen M (1958) Beta-Fe2O3 - Eine Neue Eisen (III) Oxyd-Struktur. Naturwissenschaften 45:542. https://doi.org/10.1007/BF00632057

Carraro G, Barreca D, Cruz-Yusta M, Gasparotto A, Maccato C, Morales J, Sada C, Sánchez L (2012) Vapor-phase fabrication of β-iron oxide nanopyramids for lithium-ion battery anodes. ChemPhysChem 13(17):3798–3801. https://doi.org/10.1002/cphc.201200588

Cornell RM, Schwertmann U (2003). The Iron Oxides. https://doi.org/10.1002/3527602097

Dadfar SM, Roemhild K, Drude NI, von Stillfried S, Knüchel R, Kiessling F, Lammers T (2019) Iron oxide nanoparticles: diagnostic, therapeutic and theranostic applications. Adv Drug Deliv Rev 138:302–325. https://doi.org/10.1016/j.addr.2019.01.005

Danno T, Nakatsuka D, Kusano Y, Asaoka H, Nakanishi M, Fujii T, Ikeda Y, Takada J (2013) Crystal structure of β-Fe2O3 and topotactic phase transformation to α-Fe2O3. Cryst Growth Des 13(2):770–774. https://doi.org/10.1021/cg301493a

Danno T, Asaoka H, Nakanishi M, Fujii T, Ikeda Y, Kusano Y, Takada J (2010) Formation mechanism of nano-crystalline β-Fe2O3 particles with bixbyite structure and their magnetic properties. J Phys Conf Ser 200:082003. https://doi.org/10.1088/1742-6596/200/8/082003

Estelrich J, Busquets MA (2018) Iron oxide nanoparticles in photothermal therapy. Molecules 23(7):1567. https://doi.org/10.3390/molecules23071567

Fragoso J, Barreca D, Bigiani L, Gasparotto A, Sada C, Lebedev OI, Modin E, Pavlovic I, Sánchez L, Maccato C (2022) Enhanced photocatalytic removal of NOx Gases by β-Fe2O3/CuO and β-Fe2O3/WO3 nanoheterostructures. Chem Eng J 430:132757. https://doi.org/10.1016/j.cej.2021.132757

Grazulis S, Chateigner D, Downs RT, Yokochi AFT, Quiro M, Lutterotti L, Manakova E, Butkus J, Moeck P, Bail AL (2009) Crystallography open database – an open-access collection of crystal structures. J Appl Crystallogr 42:726–729. https://doi.org/10.1107/S0021889809016690

Gregor C, Hermanek M, Jancik D, Pechousek J, Filip J, Hrbac J, Zboril R (2010) The effect of surface area and crystal structure on the catalytic efficiency of iron(III) oxide nanoparticles in hydrogen peroxide decomposition. Eur J Inorg Chem 2010(16):2343–2351. https://doi.org/10.1002/ejic.200901066

Hermanek M, Zboril R (2008) Polymorphous exhibitions of iron(III) oxide during isothermal oxidative decompositions of iron salts: a key role of the powder layer thickness. Chem Mater 20(16):5284–5295. https://doi.org/10.1021/cm8011827

Ikeda Y, Takano M, Bando Y (1986) Formation mechanism of needle-like α-Fe2O3 particles grown along the c axis and characterization of precursorily formed β-Fe2O3. Bull Inst Chem Res,

Kyoto University 64 (4): 249–58. http://hdl.handle.net/2433/77155.
Jin J, Ohkoshi SI, Hashimoto K (2004) Giant Coercive Field of Nanometer-Sized Iron Oxide. Adv Mater 16(1):48–51. https://doi.org/10.1002/adma.200305297
Klencsár Z, Kuzmann E, Vértes A (1996) User-friendly software for Mössbauer spectrum analysis. J Radioanal Nucl Chem 210(1):105–118. https://doi.org/10.1007/bf02055410
Kumar A, Singhal A (2007) Synthesis of colloidal β-Fe2O3 nanostructures - influence of addition of Co2+ on their morphology and magnetic behavior. Nanotechnology. https://doi.org/10.1088/0957-4484/18/47/475703
Kumar A, Singhal A (2009) Synthesis of colloidal silver iron oxide nanoparticles - study of their optical and magnetic behavior. Nanotechnology. https://doi.org/10.1088/0957-4484/20/29/295606
Lee JS, Im SS, Lee CW, Yu JH, Choa YH, Oh ST (2004) Hollow nanoparticles of β-iron oxide synthesized by chemical vapor condensation. J Nanopart Res 6(6):627–631. https://doi.org/10.1007/s11051-004-6322-8
Lee CW, Jung SS, Lee JS (2008a) Phase transformation of β-Fe2O3 hollow nanoparticles. Mater Lett 62(4–5):561–563. https://doi.org/10.1016/j.matlet.2007.08.073
Lee CW, Lee KW, Lee JS (2008b) Optoelectronic properties of β-Fe2O3 hollow nanoparticles. Mater Lett 62(17–18):2664–2666. https://doi.org/10.1016/j.matlet.2008.01.008
Li Y, Luo N, Sun G, Zhang B, Ma G, Jin H, Wang Y, Cao J, Zhang Z (2018) Facile synthesis of $ZnFe_2O_4$/α-Fe_2O_3 porous microrods with enhanced TEA-sensing performance. J Alloy Compd 737:255–262. https://doi.org/10.1016/j.jallcom.2017.12.068
Li Y, Zhang N, Liu C, Zhang Y, Xu X, Wang W, Feng J, Li Z, Zou Z (2021) Metastable-phase β-Fe2O3 photoanodes for solar water splitting with durability exceeding 100h. Chin J Catal 42(11):1992–1998. https://doi.org/10.1016/S1872-2067(21)63822-6
Lutterotti L (2010) Total pattern fitting for the combined size-strain-stress-texture determination in thin film diffraction. Nucl Instrum Methods Phys Res, Sect B 268(3–4):334–340. https://doi.org/10.1016/j.nimb.2009.09.053
Machala L, Zboril R, Gedanken A (2007) Amorphous iron(III) oxide-a review. J Phys Chem B 111(16):4003–4018. https://doi.org/10.1021/jp064992s
Machala L, Tuček J, Zbořil R (2011) Polymorphous transformations of nanometric iron(III) oxide: a review. Chem Mater 23(14):3255–3272. https://doi.org/10.1021/cm200397g
Machala L, Zoppellaro G, Tuček J, Šafářová K, Marušák Z, Filip J, Pechoušek J, Zbořil R (2013) Thermal decomposition of prussian blue microcrystals and nanocrystals-iron(III) oxide polymorphism control through reactant particle size. RSC Adv 3(42):19591–19599. https://doi.org/10.1039/c3ra42233j
Malina O, Kaslik J, Tucek J, Cuda J, Medrik I, Zboril R (2014) Thermally-induced solid state transformation of β-Fe2O3 nanoparticles in various atmospheres. AIP Conf Proc 1622(2014):89–96. https://doi.org/10.1063/1.4898615
Malina O, Tuček J, Jakubec P, Kašlík J, Medřík I, Tokoro H, Yoshikiyo M, Namai A, Ohkoshi SI, Zbořil R (2015) Magnetic ground state of nanosized β-Fe2O3 and its remarkable electronic features. RSC Adv 5(61):49719–49727. https://doi.org/10.1039/c5ra07484c
Malina O, Jakubec P, Kaslik J, Tucek J, Zbořil R (2017) A Simple high-yield synthesis of high-purity Hägg Carbide (χ-Fe5C2) nanoparticles with extraordinary electrochemical properties. Nanoscale 9:10440–10446. https://doi.org/10.1039/c7nr02383a
Mohapatra M, Anand S (2011) Synthesis and applications of nanostructured iron oxides/hydroxides: a review. Int J Eng Sci Technol 2(8):127–146. https://doi.org/10.4314/ijest.v2i8.63846
Momma K, Izumi F (2011) VESTA 3 for three-dimensional visualization of crystal, volumetric and morphology data. J Appl Crystallogr 44(6):1272–1276. https://doi.org/10.1107/S0021889811038970
Novák P, Procházka V, Stejskal A (2022) Universal drive unit for detector velocity modulation in mössbauer spectroscopy. Nuclear Inst Methods Phys Res Sect A Accel Spectrom Detect Assoc Equip 1031:166573. https://doi.org/10.1016/j.nima.2022.166573
Procházka V, Novák P, Vrba V, Stejskal A, Dudka M (2020) Autotuning procedure for energy modulation in Mössbauer spectroscopy. Nucl Instrum Methods Phys Res, Sect B 483(August):55–62. https://doi.org/10.1016/j.nimb.2020.08.015
Rahman MM, Jamal A, Khan SB, Faisal M (2011) Characterization and applications of as-grown β-Fe2O3 nanoparticles prepared by hydrothermal method. J Nanopart Res 13(9):3789–3799. https://doi.org/10.1007/s11051-011-0301-7
Ramya SIS, Mahadevan CK (2012) Preparation by a simple route and characterization of amorphous and crystalline Fe2O3 nanophases. Mater Lett 89:111–114. https://doi.org/10.1016/j.matlet.2012.08.090
Sakurai S, Namai A, Hashimoto K, Ohkoshi S (2009) First observation of phase transformation of all four Fe2O3 phases (γ - ε - β - α-phase). J Am Chem Soc 29:18299–18303. https://doi.org/10.1021/ja9046069
Siriwardane RV, Poston JA, Fisher EP, Shen M, Miltz AL (1999) Decomposition of the sulfates of copper, iron (II), iron (III), nickel, and zinc: XPS, SEM, DRIFTS, XRD, and TGA study. Appl Surf Sci 152(3–4):219–236. https://doi.org/10.1016/S0169-4332(99)00319-0
Sivula K, LeFormal F, Grätzel M (2011) Solar water splitting: progress using hematite (α-Fe2O3) photoelectrodes. Chemsuschem 4:432–449. https://doi.org/10.1002/cssc.201000416
Tagawa H (1984) Thermal decomposition temperatures of metal sulfates. Thermochim Acta 80:23–33. https://doi.org/10.1016/0040-6031(84)87181-6
Tokoro H, Namai A, Ohkoshi S (2020) Advances in magnetic films of ε-iron oxide toward next- generation high-density recording media. Dalton Trans 50(50):452–459. https://doi.org/10.1039/d0dt03460f
Tuček J, Zbořil R, Namai A, Ohkoshi S (2010) ε-Fe2O3: an advanced nanomaterial exhibiting giant coercive field, millimeter-wave ferromagnetic resonance, and magnetoelectric coupling. Chem Mater 22(24):6483–6505. https://doi.org/10.1021/cm101967h
Zboril R, Mashlan M, Krausova D, Pikal P (1999b) Cubic β-Fe2O3 as the product of the thermal decomposition of Fe2(SO4)3. Hyperfine Interact 120–121(1–8):497–501. https://doi.org/10.1023/A:1017018111071
Zboril R, Mashlan M, Petridis D (2002) Iron(III) oxides from thermal processes-synthesis, structural and magnetic properties, mössbauer spectroscopy characterization, and applications. Chem Mater 14(3):969–982. https://doi.org/10.1021/cm0111074
Zboril R, Mashlan M, Papaefthymiou V, Hadjipanayis G (2003) Thermal decomposition of Fe2(SO4)3: demonstration of Fe2O3 polymorphism. J Radioanal Nucl Chem 255(3):413–417. https://doi.org/10.1023/A:1022543323651
Zboril R, Mashlan M, Krausova D (1999a) The mechanism of β-Fe2O3 formation by solid-state reaction between NaCl and Fe2(SO4)3. In: Miglierini, M, Petridis D (eds) Mössbauer spectroscopy in materials science, vol. 2, pp. 49–56. https://doi.org/10.1007/978-94-011-4548-0_5. Springer, Dordrecht
Zhang N, Guo Y, Wang X, Zhang S, Li Z, Zou Z (2017) A Beta-Fe2O3 nanoparticle-assembled film for photoelectrochemical water splitting. Dalton Trans 46(32):10673–10677. https://doi.org/10.1039/c7dt00900c
Zhang Y, Zhang N, Wang T, Huang H, Chen Y, Li Z, Zou Z (2019) Heterogeneous degradation of organic contaminants in the

photo-fenton reaction employing pure cubic β-Fe2O3. Appl Cataly B Environ 245:410–419. https://doi.org/10.1016/j.apcatb.2019.01.003

Zhang N, Guo Y, Huang H, Yan S, Li Z, Zou Z (2022) Onset potential shift of water oxidation in the metastable phase transformation process of β-Fe_2O_3. Energ Fuels 36(19):11567–11575. https://doi.org/10.1021/acs.energyfuels.2c01812